

Probing component contributions and internal polarization in silicon-graphite composite anode for lithium-ion batteries with an electrochemical-mechanical model

Yue Chen(陈约), Fuliang Guo(郭福亮), Lufeng Yang(杨陆峰), Jiaze Lu(卢嘉泽),Danna Liu(刘丹娜), Huayu Wang(王华宇), Jieyun Zheng(郑杰允), Xiqian Yu(禹习谦), and Hong Li(李泓)

Citation: Chin. Phys. B, 2022, 31 (**7**): 078201. DOI: 10.1088/1674-1056/ac6012
Journal homepage: http://cpb.iphy.ac.cn; http://iopscience.iop.org/cpb

What follows is a list of articles you may be interested in

Lithium ion batteries cathode material: V_2O_5

Baohe Yuan(袁保合), Xiang Yuan(袁祥), Binger Zhang(张冰儿), Zheng An(安政), Shijun Luo(罗世钧), and Lulu Chen(陈露露)

Chin. Phys. B, 2022, 31 (**3**): 038203. DOI: 10.1088/1674-1056/ac21be

Analysis on diffusion-induced stress for multi-layer spherical core-shell electrodes in Li-ion batteries

Siyuan Yang(杨思源), Chuanwei Li(李传崴), Zhifeng Qi(齐志凤), Lipan Xin(辛立攀), Linan Li(李林安), Shibin Wang(王世斌), and Zhiyong Wang(王志勇)

Chin. Phys. B, 2021, 30 (**9**): 098201. DOI: 10.1088/1674-1056/ac11de

In situ formed FeS_2@CoS cathode for long cycling life lithium-ion battery

Xin Wang(王鑫), Bojun Wang(汪博筠), Jiachao Yang(杨家超), Qiwen Ran(冉淇文), Jian Zou(邹剑), Pengyu Chen(陈鹏宇), Li Li(李莉), Liping Wang(王丽平), and Xiaobin Niu(牛晓滨)

Chin. Phys. B, 2021, 30 (**8**): 088201. DOI: 10.1088/1674-1056/abe9ab

Rules essential for water molecular undercoordination

Chang Q Sun(孙长庆)

Chin. Phys. B, 2020, 29 (**8**): 088203. DOI: 10.1088/1674-1056/ab8dad

Size effects in lithium ion batteries

Hu-Rong Yao(姚胡蓉), Ya-Xia Yin(殷雅侠), Yu-Guo Guo (郭玉国)

Chin. Phys. B, 2016, 25 (**1**): 018203. DOI: 10.1088/1674-1056/25/1/018203

Probing component contributions and internal polarization in silicon-graphite composite anode for lithium-ion batteries with an electrochemical-mechanical model

Yue Chen(陈约)[1,2], Fuliang Guo(郭福亮)[1,2], Lufeng Yang(杨陆峰)[1], Jiaze Lu(卢嘉泽)[1], Danna Liu(刘丹娜)[3], Huayu Wang(王华宇)[4,5], Jieyun Zheng(郑杰允)[1], Xiqian Yu(禹习谦)[1], and Hong Li(李泓)[1,2,3,5,†]

[1] *Beijing Advanced Innovation Center for Materials Genome Engineering, Key Laboratory for Renewable Energy, Beijing Key Laboratory for New Energy Materials and Devices, Institute of Physics, Chinese Academy of Sciences, Beijing* 100190, *China*

[2] *School of Physical Sciences, University of Chinese Academy of Sciences, Beijing* 100049, *China*

[3] *Beijing WeLion New Energy Technology Co., Ltd., Beijing* 100176, *China*

[4] *Li Auto Inc., Beijing* 101399, *China*

[5] *Tianmu Lake Institute of Advanced Energy Storage Technologies, Liyang* 213300, *China*

(Received 10 January 2022; revised manuscript received 14 February 2022; accepted manuscript online 23 March 2022)

Silicon–graphite (Si–Gr) composite anodes are attractive alternatives to replace Gr anodes for lithium-ion batteries (LIBs) owing to their relatively high capacity and mild volume change. However, it is difficult to understand electrochemical interactions of Si and Gr in Si–Gr composite anodes and internal polarization of LIBs with regular experiment methods. Herein, we establish an electrochemical-mechanical coupled model to study the effect of rate and Si content on the electrochemical and stress behavior in a Si–Gr composite anode. The results show that the composites of Si and Gr not only improve the lithiation kinetics of Gr but also alleviate the voltage hysteresis of Si and decrease the risk of lithium plating in the negative electrode. What's more, the Si content is a tradeoff between electrode capacity and electrode volume variation. Further, various internal polarization contributions of cells using Si–Gr composite anodes are quantified by the voltage decomposition method. The results indicate that the electrochemical polarization of electrode materials and the electrolyte ohmic over-potential are dominant factors in the rate performance of cells, which provides theoretical guidance for improving the rate performance of LIBs using Si–Gr composite anodes.

Keywords: Si–Gr, electrochemical interactions, polarization, rate performance

PACS: 82.47.Aa, 65.40.gk, 82.45.Fk **DOI:** 10.1088/1674-1056/ac6012

1. Introduction

The strong demand for electric mobility is driving the development of lithium-ion batteries (LIBs) with high energy density,[1] which needs to exploit cathode and anode with high capacity. For the cathode side, some strategies such as transition metal doping and coating are employed to improve the practical capacity of layered cathode materials, such as $LiNi_{1-x-y}Co_xMn_yO_2$ and spinel $LiMn_2O_4$.[2–5] As for the anode side, introducing Si or silicon oxide as an additive is the main solution to improve the capacity of Gr in industry. The iterative upgrade of the anode is one of the drivers for improvement of battery energy density, because it decreases the proportion of inert materials and increases charge cut-off voltage. For example, adding 6 wt% Si into Gr anode can increase 18% of the specific energy density.[6]

However, due to the huge volume change of Si (300%), the Si–Gr composite anode suffers a swelling issue at the cell level and thus it can lead to capacity degradation. In addition, it involves a complicated question for design of high-performance Si–Gr composite anodes, as the electrode behavior is a result of the coupled performance of the individual active materials. It is generally known that Gr is active mainly below 0.25 V versus Li/Li^+, whereas Si is active in the range 0–1 V. Thus, it is challenging to quantify the intra-electrode process through experiments due to the partial overlap of Si and Gr equilibrium potential during lithiation and delithiation. Recently, considerable efforts have been devoted to figuring out this question. For example, Abraham *et al.* and Yao *et al.* have quantified the lithiation and delithiation behavior of Si–Gr composite anodes by energy-dispersive x-ray diffraction[7] and operando x-ray scattering.[8] Richter *et al.* have used operando neutron scattering and an analytical approach to investigate degradation mechanisms of Si–Gr composite anodes.[9,10] Heubner *et al.* have captured the component-specific behaviors by designing a model-like Si–Gr composite anode.[11]

Nevertheless, the component-specific electrochemical behavior and internal dynamics of the Si–Gr composite anode cannot be fully understood through the experimental method. Therefore, it is still necessary to gain more fundamental insights into the intra-electrode process of Si–Gr composite anodes with the simulation method. Porous electrode models for

†Corresponding author. E-mail: hli@iphy.ac.cn

© 2022 Chinese Physical Society and IOP Publishing Ltd

pure Si and Gr electrodes have been used to study the effect of charge and discharge rate on electrode performance.[12,13] The phase-field models have been developed to explain the complex electrochemistry behavior due to phase transition.[14,15] As for the modeling of Si–Gr composite anodes, some recent models focus on the mechanical behavior of composite anodes.[16–18] However, very few theoretical studies examine the (de)lithiation competition between Si and Gr and polarization of the cell with Si–Gr composite anodes.[19]

In this work, we present an electrochemical-mechanical model to investigate the electrochemical and stress behavior of the LIBs with Si–Gr anodes by analyzing the individual electrochemical behavior of Si and Gr. The model is validated by the experimental data of Si–Gr 550/$LiNi_{0.8}Mn_{0.1}Co_{0.1}O_2$ (NMC811) cells. The state of charge (SOC) and state of lithiation (SOL) of Si and Gr are analyzed. The effects of the current rate and Si content in the Si–Gr composite anode on the electrochemical and Li plating behavior of the composite anode is also discussed. Finally, we explore the rate performance bottleneck of the Si-based LIBs by the voltage decomposition method.

2. Methodology

2.1. The electrochemical-mechanical coupled model

Figure 1(a) illustrates the electrochemical-mechanical model coupling between particle and cell level. Specifically, electrochemistry and mechanics are coupled through interaction between the solid lithium concentration that affects stress and the hydrostatic stress that influences solid diffusion at the particle level. The Si–Gr composite anode is decoupled into an independent active material to distinguish the individual contribution of the electrochemistry and mechanics between Si and Gr. At the cell level, electrochemistry and mechanics are coupled by the interaction between the average concentration of solid phase that affects stress and volume change of the cell and stress impacting the equilibrium electrode potential of the active materials and liquid phase polarization.[20] As for the connection between particle and electrode level, it is described through the homogenizing porous electrode theory.

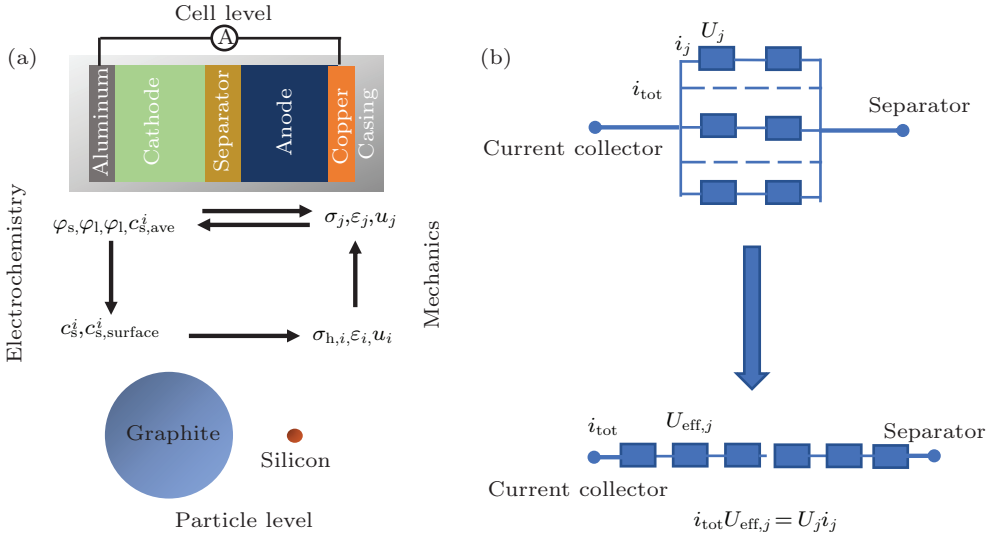


Fig. 1. Illustration of the coupled electrochemical-mechanical model using Si–Gr composite anode. (a) Schematic of the electrochemical-mechanical coupled model between particle and cell level with the Si–Gr composite anode. (b) Simplified processing diagram of the particle in the model.

2.2. The electrochemical model

In this work, the P2D model developed by Newman and Doyle is employed as the main framework of the electrochemical model.[21] Table 1 summarizes the governing equations based on the P2D model. They are presented into four physical processes: (1) the mass conservation of Li in the solid phase, which allows to follow the Li-ion concentration in the solid phase c_s, (2) the Li-ion concentration c_l in the liquid phase described by mass conservation, (3) charge balance in the solid phase and liquid phase to account for the evolution of the potential in the solid phase and liquid phase, (4) the Butler–Volmer equation used to simulate the transfer of charge at the active particle/electrolyte surface. Through them, the exchange current density of active materials is evaluated.

For the Si–Gr composite anode, Si and Gr mix in the anode. The variables and parameters of the composite anode are named for Si and Gr, respectively.

The volume fraction of the active phase in the anode can be expressed as

$$\varepsilon_{s,anode} = \varepsilon_{s,Si} + \varepsilon_{s,Gr}, \tag{1}$$

where $\varepsilon_{s,Si}$ and $\varepsilon_{s,Gr}$ represent the volume fraction of Si and Gr.

Then, the solid phase flux of Si and Gr can be expressed as

$$j_{s,i} = -\frac{D_{s,i}c_i}{RT}\nabla\mu_{s,i}. \tag{2}$$

The chemical potential considering the influence of mechanical stress on the electrochemical potential can be expressed as

$$\mu_{s,i} = \mu_{c,i}(c_s) - \Omega_i \sigma_{h,i}, \tag{3}$$

where $D_{s,i}$ are the lithium diffusion coefficients, $c_{s,i}$ are the Li concentration in the particle, R is the gas constant, T is the temperature, $\mu_{s,i}$ are the chemical potential, $\mu_{c,i}$ are the chemical potential at the stress-free state, Ω_i are partial molar volume of for each active component (such as Si, Gr, and NMC811), $\sigma_{h,i}$ is the hydrostatic pressure. As is known, $\mu_{c,i}$ is related to the open circuit potential (OCP) $E_{ref,i}$, written as

$$\mu_{c,i} = \mu^0_{Li} - FE_{ref,i}. \tag{4}$$

The solid phase Li flux can be further simplified to

$$j_{s,i} = \frac{D_{s,i}c_{s,i}}{RT}\left(\frac{F}{c_{max,i}} \cdot \frac{\partial E_{ref,i}}{\partial x_{s,i}}\nabla c_{s,i} + \nabla(\sigma_{h,i} \cdot f_{V,i}(c_i))\right), \tag{5}$$

where μ^0_{Li} is the chemical potential of Li metal, F is Faraday's constant; $c_{max,i}$ is the maximum Li concentration in the active particles, $x_{s,i}$ is the lithium fraction inside the active particles. $f_{V,i}$, and $\sigma_{h,i}$ are the intercalation-induced eigen chemical strain and hydrostatic stress.

For spherical particles, the equation of concentration distribution can be simplified as a spherical symmetry problem,

$$\frac{\partial c_{s,i}}{\partial t} + \frac{1}{r_i^2}\frac{\partial r_i^2 j_{s,i}}{\partial r_i} = 0. \tag{6}$$

The initial conditions and the boundary conditions are

$$c_{Si}(t=0) = c_{Si,0}, \quad c_{Gr}(t=0) = c_{Gr,0}, \tag{7}$$

$$j_{Si} = i_{loc,Si}/F, \quad j_{Gr} = i_{loc,Gr}/F, \tag{8}$$

$$i_{anode} = a_{Si}i_{loc,Si} + a_{Gr}i_{loc,Gr}, \tag{9}$$

where i_{anode} is current density in the anode; $i_{loc,Si}$ and $i_{loc,Gr}$ are local exchange current densities of Si and Gr particles, respectively; a_{Si} and a_{Gr} are the active material specific interfaces of the Si and Gr particles, respectively.

Table 1. The P2D model equations used in the present model.

Equation name	Equation	Boundary conditions and initial value
Conservation of Li in the particle	$\frac{\partial c_s}{\partial t} - \nabla \cdot (D_s \nabla c_s) = 0$	$c_s\|_{t=0} = c_{s,0}$ $D_s \nabla c_s\|_{r=0} = 0$ $-FD_s \nabla c_s\|_{r=r_s} = j_{in}$
Conservation of mass in the electrolyte	$\frac{\partial \varepsilon_l c_l}{\partial t} = \nabla \cdot (D_{eff} \nabla c_l) + (1-t_+)\frac{\nabla \cdot i_l}{F}$	$c_l\|_{t=0} = c_{l,0}$ $D_{eff}\nabla c_l\|_{Al/Cathode} = D_{eff}\nabla c_l\|_{Cu/Anode} = 0$
Current density in the liquid phase	$i_l = -\kappa_{eff}\nabla \phi_l + \frac{2\kappa_{eff}RT}{F}(1-t_+)\nabla Inc_l$	$i_l\|_{Al/Separator} = i_l\|_{Separator/Anode} = i$
Conservation of mass	$\nabla \cdot i_l = a_p i_{loc} + a_s C_{dl}\frac{\partial(\phi_s - \phi_l)}{\partial t}$	$i_l\|_{Al/Cathode} = i_l\|_{Cu/Anode} = 0$
Conservation of charge	$\nabla \cdot i_l + \nabla \cdot i_s = 0$	
Charge, solid phase	$i_s = -\sigma_{eff}\nabla \phi_s$	$i_s\|_{Al/Separator} = i_s\|_{Separator/Anode} = 0$ $i_s\|_{Al/Cathode} = i_s\|_{Cu/Anode} = i$
Butler–Volmer equation	$i_{loc} = i_0\left\{\exp\left[\frac{(1-\beta)F\eta}{RT}\right] - \exp(-\frac{\beta F\eta}{RT})\right\}$	
Exchange current density	$i_0 = Fk_c^{a\alpha}k_a^{a_c}(c_{s,max} - c_{s,surf})(c_{s,surf})^{\alpha_c}(\frac{c_e}{c_{c,ref}})^{\alpha_a}$	

As for the transport of Li-ion in the electrolyte, the governing equation of mass conservation of Li in the liquid phase in Table 1 can be used to follow the evolution of Li-ion concentration in the Si based anode systems. Considering the influence of volume change during (dis)charge on liquid phase diffusion, the electrolyte effective diffusion coefficient reads

$$D_{eff,l} = \frac{D_l \varepsilon_l}{\tau}, \tag{10}$$

further by the Bruggeman relation

$$D_{eff,l} = D_l \varepsilon_l^{1.5}, \tag{11}$$

where D_l, ε_l, and τ are the liquid diffusion coefficient, liquid volume fraction and tortuosity in the liquid phase.

2.2.1. Mechanical model

2.2.1.1. Continuum scale

The heterogeneous model considering the mechanical response of each component of the cell is used to describe the mechanical behavior at the cell level. Assuming that the deformation of each component conforms to the linear elastic constitutive relationship, the stress of the single component in the cell is given by

$$\Sigma_{ij} = C_{ijkl}(e_{kl} - e^c\delta_{kl}), \tag{12}$$

where i contain casing, copper, anode, separator, cathode, and aluminum; Σ_{ij}, C_{ijkl}, and e^c are the stress tensor, the elastic stiffness tensor of components and the chemical strains in the cell; δ_{kl} is Kronecker delta tensor. It is supposed that the chemical strains generated during charge and discharge only contribute to the thickness of the electrode, which is reasonable because the electrode is constrained by the current collector. Thus, each component's chemical strain tensor of anode and cathode in the electrode's thickness direction can be expressed as

$$e^c_{anode} = \varepsilon_{Si}f_{V,Si}(c_{Si,average}) + \varepsilon_{Gr}f_{V,Gr}(c_{Gr,average}), \tag{13}$$

$$e^c_{cathode} = \varepsilon_{NCM}f_{V,NCM}(c_{NCM,average}), \tag{14}$$

and the chemical strain of the electrode parallel to the direction of the current collector can be denoted by

$$e^{\mathrm{c}}_{\mathrm{anode}} = 0, \tag{15}$$

$$e^{\mathrm{c}}_{\mathrm{cathode}} = 0, \tag{16}$$

where $\varepsilon_{\mathrm{NCM}}$ is the volume fraction of NCM811 in the positive electrode; $f_{\mathrm{V,Si}}$, $f_{\mathrm{V,Gr}}$, and $f_{\mathrm{V,NCM}}$ represent the intercalation-induced eigen chemical strain of Si, Gr, and NCM811. The eigen chemical strain is a function of Li-ion concentration, as shown in Figs. S2(a)–S2(b) in the supplementary information.

The equilibrium of macroscopic stress gives

$$\nabla \cdot \Sigma = 0. \tag{17}$$

As for the calculation of electrode porosity, we have

$$\frac{\Delta V}{V_0} = f, \tag{18}$$

$$\Delta V_{\mathrm{active}} + \Delta V_{\mathrm{binder}} + \Delta V_{\mathrm{liquild}} = fV_0, \tag{19}$$

$$\begin{aligned} \varepsilon_{\mathrm{liquid}} &= \frac{\varepsilon^0_{\mathrm{liquid}} V_0 + fV_0 - \Delta V_{\mathrm{active}} - \Delta V_{\mathrm{binder}}}{V_0(1+f)} \\ &\approx \frac{\varepsilon^0_{\mathrm{liquid}} V_0 + fV_0 - \Delta V_{\mathrm{active}}}{V_0(1+f)}, \end{aligned} \tag{20}$$

$$\varepsilon_{\mathrm{active}} = \frac{\varepsilon^0_{\mathrm{active}} V_0 + \Delta V_{\mathrm{active}}}{V_0(1+f)}, \tag{21}$$

where f, ΔV, V_0 represent the volume change ratio, volume change and pristine electrode volume; $\Delta V_{\mathrm{active}}$, $\Delta V_{\mathrm{binder}}$, and $\Delta V_{\mathrm{liquid}}$ are the volume change of active materials, binder phase and liquid phase in each electrode; $\varepsilon^0_{\mathrm{liquid}}$ and $\varepsilon_{\mathrm{liquid}}$ are the liquid phase volume fraction of initial and lithiation states; $\varepsilon^0_{\mathrm{active}}$ and $\varepsilon_{\mathrm{active}}$ are the solid phase volume fraction of initial and lithiation states.

The boundary conditions and initial conditions are

$$u(x,y) = 0 \quad \text{at} \quad y = 0, \tag{22}$$

$$u(x,y) = 0, \quad \frac{\partial u}{\partial t} = 0. \tag{23}$$

2.2.1.2. Microscale

In this work, a mechanical model of particle scale[22,23] is used to investigate stress distribution and displacement of particles. For a spherical particle, the equilibrium equation can be degraded into a typical spherical symmetry problem as

$$\frac{\mathrm{d}\sigma_r}{\mathrm{d}r} + \frac{2}{r}(\sigma_r - \sigma_\theta) = 0. \tag{24}$$

The constitutive relation based on linear elasticity gives

$$\sigma_{ij} = 2Ge_{ij} + \lambda e_{kk}\delta_{ij} - \frac{E}{1-2v} f(c_{\mathrm{average}})\delta_{ij}, \tag{25}$$

where σ_{r} and σ_θ are the normal stress and radial stress; r is the radius of the particle; G, λ, δ_{ij}, E, and v denote the shear modulus, Lame constant, the Kronecker delta function, elastic modulus, and Poisson's ratio. The boundary conditions are

$$u(r=0) = 0, \quad \sigma_{\mathrm{r}}(r = r_{\mathrm{p}}) = 0, \tag{26}$$

$$u_{\mathrm{r},i} = \{[1 + f_{\mathrm{V},i}(c_{\mathrm{average},i})]^{1/3} - 1\} r_{\mathrm{p},i}, \quad \text{at} \quad r = r_{\mathrm{p},i}, \tag{27}$$

where r_{p} denotes the initial particle size of Si and Gr.

2.2.2. Analysis of the polarization in a Li-ion battery

A polarization decomposition method that enables both quantification and localization of the polarization in a battery cell is applied by calculating directly from the potential and concentration profiles in the cell.[24] The polarization inside the battery can be divided into anode, separator, and cathode. The polarization includes electrolyte diffusion, electrolyte ohmic, solid phase ohmic, active material diffusion, and activation overpotential in the electrode. These polarizations are connected in series and parallel inside the electrode, as shown in Fig. 1(b). To obtain these polarizations, they can be equivalently connected in series under the condition that the power of every polarization is same. Thus, the polarization inside the battery can be divided into diffusion polarization of electrolyte, ohmic potential drop of electrolyte, liquid phase polarization, diffusion polarization of solid phase, activation overpotential.

Specifically, diffusion polarization of electrolyte can be denoted as

$$-\frac{1}{j_{tot}} \iint \frac{2RT}{c_{\mathrm{l}}F} \cdot (1 + t^0_+) \cdot \left(1 + \frac{\partial Inf_\pm}{\partial Inc_{\mathrm{l}}}\right) \cdot j_{\mathrm{l}} \mathrm{d}x\mathrm{d}y, \tag{28}$$

where j_{tot} and j_{l} are the total current and liquid phase current per cross-sectional area; c_{l}, t^0_+, and $f_\pm$ are the Li-ion concentration, Li-ion transference number, and mean molar activity coefficient of the electrolyte phase.

The ohmic potential drop of the electrolyte can be expressed as

$$\frac{1}{j_{\mathrm{tot}}} \iint \frac{j^2_{\mathrm{l}}}{k_{\mathrm{eff}}} \mathrm{d}x\mathrm{d}y, \tag{29}$$

where k_{eff} is the effective lithium-ion conductivity of the electrolyte.

Liquid phase polarization can be expressed as

$$-\frac{1}{j_{\mathrm{tot}}} \iint \frac{2RT}{c_{\mathrm{l}}F} k_{\mathrm{c}} \frac{\partial c_{\mathrm{l}}}{\partial x} j_{\mathrm{l}} \mathrm{d}x\mathrm{d}y + \frac{1}{j_{\mathrm{tot}}} \iint \frac{j^2_{\mathrm{l}}}{k_{\mathrm{eff}}} \mathrm{d}x\mathrm{d}y. \tag{30}$$

Diffusion polarization of solid phase can be expressed as

$$\frac{1}{j_{\mathrm{tot}}} \iint a j_{\mathrm{loc}} (E_{\mathrm{surf}} - \mathrm{E_{ave}}) \mathrm{d}x\mathrm{d}y. \tag{31}$$

Activation overpotential can be expressed as

$$\frac{1}{j_{\mathrm{tot}}} \iint a j_{\mathrm{loc}} (\varphi_{\mathrm{s}} - \varphi_{\mathrm{l}} - E_{\mathrm{surf}}) \mathrm{d}x\mathrm{d}y, \tag{32}$$

where a and j_{loc} are the specific area of the active material particles and the local current per active material area. E_{surf} and E_{ave} are the superficial and average electrode potential of the active material.

The interface overpotential can be expressed as

$$\frac{1}{j_{\text{tot}}}\iint a j_{\text{loc}}(E_{\text{surf}}-\text{E}_{\text{ave}})\,\text{d}x\,\text{d}y + \frac{1}{j_{\text{tot}}}\iint a j_{\text{loc}}(\varphi_{\text{s}}-\varphi_{\text{l}}-E_{\text{surf}})\,\text{d}x\,\text{d}y, \tag{33}$$

where φ_{s} and φ_{l} are the solid phase potential and liquid phase potential.

The above equation is solved using COMSOL Multiphysics®5.5. A two-dimensional geometric model ($L = 100d$) is used to simulate the geometric structure of the lithium-ion battery soft pack cell as shown in Fig. S1. The electrochemical model can be carried out by the LIB module and the mechanical model can be carried out by solid mechanics in COMSOL Multiphysics. In the electrochemical model, the positive electrode material is NCM811, the negative electrode material is Si and Gr, the electrolyte is 1 mol·dm^{-3} $LiPF_6$ in EC (ethylene carbonate)/DEC (diethyl carbonate) (1/1, V/V), and the material parameters are shown in Table 2. Figure S1 shows that the copper collector boundary is ground and the aluminum collector boundary is applied with current density as the same as the experiment current condition. Moreover, the casing boundary is fixed.

Table 2. Technological parameters of electrodes.

Parameter	Design value
Positive electrode	
Active material ratio (wt%)	98
Unilateral areal density (g·m^{-2})	230
Press density (g·m^{-3})	3.45
Binder ratio (wt%)	1.8
Conductive agent ratio (wt%)	0.2
Reversible capacity (mAh·g^{-1})	199
Negative electrode	
Active material ratio (wt%)	95
Unilateral areal density (g·m^{-2})	100
Press density (g·m^{-3})	1.6
Binder ratio (wt%)	3
Conductive agent ratio (wt%)	2
Reversible capacity (mAh·g^{-1})	531
n/p ratio	1.1

Table 3. Material parameters used in the model.

Parameter	Value	References
Positive electrode		
The initial radius of NCM (μm)	5.395	Estimated
Solid phase lithium diffusivity (m^2·s^{-1})	3×10^{-13}	[25]
Solid phase electronic conductivity (S·m^{-1})	0.17	[25]
Maximum concentration (mol·m^{-3})	50060	[25]
Open circuit voltages (V)	Fig. S2(a)	Measured
Reaction rate of NCM (m·s^{-1})	3×10^{-11}	[25]
Young's modulus of the cathode (MPa)	182	[16]
Young's modulus of NCM (GPa)	140	[16]
The volume change of NCM	Fig. S1	[26]
Young's modulus of Al (GPa)	70	[27]
Negative electrode		
The initial radius of Si (nm)	50	Estimated
The initial radius of Gr (μm)	6.45	Measured
Active material volume fraction (Si)	0.0452	Estimated
Active material volume fraction (Gr)	0.63	Estimated
Solid phase lithium diffusivity of Si (m^2·s^{-1})	2×10^{-16}	[28]
Solid phase lithium diffusivity of Gr (m^2·s^{-1})	3×10^{-14}	[25]
Solid phase electronic conductivity of anode (S·m^{-1})	5	[27]
The maximum concentration of Gr (mol·m^{-3})	31924	Estimated
The maximum concentration of Si (mol·m^{-3})	308940	Estimated
Open circuit voltages of Si (V)	Fig. S3(b)	Measured
Open circuit voltages of Gr (V)	Fig. S3(a)	[16]
Reaction rate of Si (m·s^{-1})	0.95×10^{-13}	Estimated
Reaction rate of Gr (m·s^{-1})	2×10^{-11}	Estimated
Young's modulus of the anode (MPa)	140	[16]
Young's modulus of separator (MPa)	262	[17]
The volume change of Si	Fig. S1	[17]
The volume change of Gr	Fig. S1	[29]
Young's modulus of Si (GPa)	$124+78x$	[16]
Young's modulus of Gr (GPa)	$19.25+82.23x$	[16]
Young's modulus of Cu (GPa)	110	[27]
Separator		
Solid phase volume fraction of separator	0.6	[16]
Young's modulus of separator (MPa)	262	[22]
Electrolyte ionic diffusivity (m^2·s^{-1})	7.5×10^{-11}	[26]
Electrolyte ionic conductivity (S·m^{-1})	f(cl)	[26]
Transference number	0.363	[26]

The physical parameters of the model in this work are obtained by experimental measurement, calculation and fitting as listed in Table 3. The estimated physical parameters of the present model are explained as follows: the D50 value of active material provided by the material manufacturer (Jiangsu Easpring material technology Co.,LTD and Tianmulake excellent anode materials Co.,LTD) is applied as the radius of the active material in the simulation model.

The active material volume fraction Si–Gr and NCM are estimated through a comparison of the theoretical electrode density and the actual density,

$$\varepsilon_{\text{act}} = \frac{m_{\text{coat}}}{L\rho}, \tag{34}$$

where ε_{act} is the active material volume fraction, and m_{coat} is the electrode coating mass per unit area.

Further, the volume fraction of Si and Gr can be calculated by

$$\varepsilon_{\text{Si}} = \varepsilon_{\text{act}} \frac{\frac{w_{\text{Si}}}{\rho_{\text{Si}}}}{\frac{w_{\text{Si}}}{\rho_{\text{Si}}} + \frac{1-w_{\text{Si}}}{\rho_{\text{Gr}}}}, \tag{35}$$

$$\varepsilon_{\text{Gr}} = \varepsilon_{\text{act}} - \varepsilon_{\text{Si}}, \tag{36}$$

$$w_{\text{Si}} = \frac{Q_{\text{Si-Gr}} - Q_{\text{Gr}}}{Q_{\text{Si}} - Q_{\text{Gr}}}. \tag{37}$$

Here w_{Si} is the mass fraction of Si in the Si–Gr composite materials; ρ_{Si} and ρ_{Gr} are the densities of Si and Gr; $Q_{\text{Si-Gr}}$, Q_{Si}, and Q_{Gr} are the specific capacities of Si–Gr composite, Si, and Gr.

In addition, the maximum concentration of Si and Gr is calculated by

$$C_{\text{Li,max}} = \frac{\rho}{M}, \tag{38}$$

where ρ and M are the density and molar mass of the active materials, respectively.

The reaction rates of Si and Gr are fitted with the experimental data. The parameter values of the model are given in Tables 2 and 3.

2.3. Experimental details

A 3 Ah pouch cell of Si–Gr 550 (5 wt% Si)/NMC811 is designed to calibrate the mechanical-electrochemical coupled model. The Si–Gr 550 and NCM811 are purchased by Jiangsu Espring material technology Co.,LTD and Tianmulake excellent anode materials Co., LTD, respectively. The parameters of electrodes are summarized in Table 2. The cell is cycled at a current rate of 0.3 C charge and 1 C discharge within 2.5–4.25 V. The OCV measurements for charge and discharge of the anode (50 nm-Si)/Li and cathode (NMC811)/Li half cells are measured. The galvanostatic intermittent titration technique is applied for anode half cells and cathode half cells.

3. Results and discussion

Based on the coupled electrochemical-mechanical model, the voltage profiles, component-specific contributions, and the pressure of the pouch cell (Si–Gr 550/NCM811) upon 1/3 C charge and 1 C discharge are calculated by COMSOL Multiphysics, as shown in Fig. 2. Figure 2(a) and Fig. S6 in supplementary information show that the simulation result is in good agreement with the results of practical experiments, which demonstrates the effectiveness of our model for the prediction of mechanics-induced electrochemical behaviors. Further, the (de)lithiation behavior of anode and cathode based on the validated model is investigated in Figs. 2(b) and 2(c). It is shown that the normalized concentration of Li in the cathode displays a linear evolution upon charge and discharge. Meanwhile, Si and Gr have a nonlinear change of their normalized Li concentration, which can be attributed to the lithiation competition between the Si and Gr in the composite anode. Specifically, the lithiation rate of Gr is slow, while Si dominates the electrode reaction at low SOC. At time = 2150 s (corresponding to SOC = 0.18), the SOC contribution of Gr in the composite anode increases. This surpasses the SOC contribution of Si at time = 6500 s (corresponding to SOC = 0.54). In addition, the SOL of Si and Gr reach 0.93 and 0.86, and the SOC of Si and Gr reach 0.38 and 0.62, respectively, at SOC = 1. This indicates that the main capacity contribution of the Si–Gr 550 anode is still Gr. During delithiation, there is a sharp separation between the two SOC regions dominated by Si (SOC = 0.38–1) and Gr (SOC = 0.07–0.38). Notably, the differences between lithiation and delithiation are due to the large voltage hysteresis of Si [Fig. S3(b)]. Figure S3(b) shows that the OCV difference of Si during the charging and discharging process under different SOL is not a constant value, and the difference increases with the decrease of SOL state. The large potential hysteresis of Si is usually attributed to the different thermodynamics caused by the bond-breaking of Si,[30] the stress,[31] and kinetic resistance.[32] Nevertheless, the results observed in this work agree well with those reported in recent literature based on the experiment method,[11] indicating that our model could effectively capture the specific component contribution in the Si–Gr composite anode.

The pressure and integrated volume change of the cells are calculated in Fig. 2(d). It can be found that the pressure and volume evolution profiles of the cell are nonlinearly caused by the difference of the component-specific volume change in the anode.[33] Notably, the average von Mises stress and volume change of the cell at the end of charge are calculated to be 1.5 MPa and 4.7%, respectively. The distribution of concentration and stress at the electrode level are also given in Figs. S4 and S5, which show that solid-phase concentration and von Mises stress are fair uniforms in each component during charge. In contrast, the solid phase concentration and von Mises stress of anode and cathode are slightly high near the separator side due to the gradient of the electrolyte concentration during discharge.

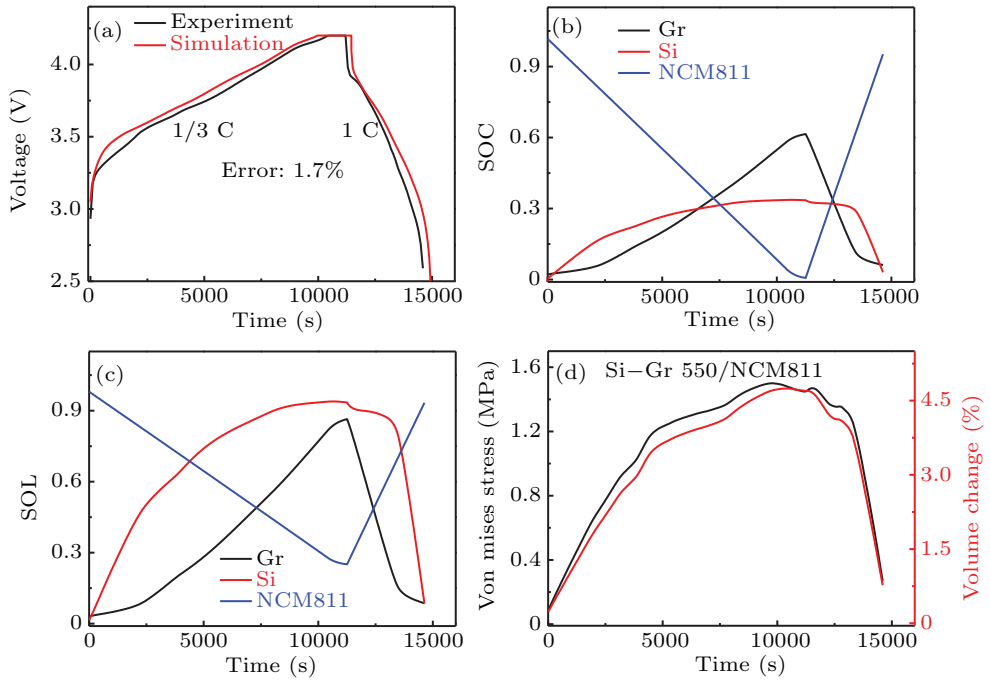


Fig. 2. Si–Gr 550/NCM811 cell modeling results with the electrochemical-mechanical coupled model: (a) the comparison of the simulation and experiment results based on Si–Gr 550/NCM811 cells, (b) the SOC of Si–Gr composite anode, (c) the SOL of Si–Gr composite anode, and (d) the pressure and volume change of cells at 0.3 C charge and 1 C discharge.

To further understand the rate capability of the Si–Gr composite anode, it is necessary to study the influence of different rates on the specific contributions of Si and Gr in the composite anode. Figure 3(a) shows that the SOL of Gr decreases significantly as the charge rate increases from 0.3 C to 2 C. The SOL of Gr at the end of charge is decreasing from 0.87 to 0.25 as the charge rate increases from 0.3 C to 2 C, which indicates that the intrinsic lithium intercalation kinetics of Gr is relatively poor.[34] Meanwhile, the SOL of Si decreases from 0.9 to 0.67, and its decline is more moderate than that of Gr (Fig. 3(b)). Correspondingly, the SOC contribution of Gr drops faster than that of Si, as shown in Figs. 3(c)–3(d), indicating that Si has a better rate capability during charge. This can be due to the Li-ion diffusion kinetics of the Si increased during charge.[35,36] During discharge, the delithiation rate of Gr drops as the discharge rate increases (Fig. 3(a)). The SOL of Gr appears to increase when SOC decreases from 0.2 to 0. This phenomenon suggests that a small amount of Li is extracted from the Si, while the Li is inserted into Gr. This internal redox mechanism in Si–Gr is evidenced by the result of operando neutron scattering measurements.[9] As for the Si component, the delithiation platform becomes shortening, and the SOL at the end of discharge increases from 0.01 to 0.28 when the discharge rate increases from 0.3 C to 2 C, respectively. Thus, it is shown that Gr has a higher rate capability than Si during discharge, which can be further confirmed by Figs. 3(c) and 3(d). In a word, the combination of Si and Gr can make up for their specific shortcomings upon charge and discharge processes to improve the comprehensive electrochemical performance of the composite anode.

Furthermore, the effects of (dis)charge rate on the stress at cell and particle level are investigated, as shown in Figs. 3(e) and 3(f). As the (dis)charge rate increases, the stress of Si and Gr increases, while the stress and volume change of the cell decrease. Such a phenomenon can be owing to the fact that the high (dis)charge rate tends to increase the heterogeneity of the lithium concentration between Si and Gr at the particle level, causing large surface von Mises stress of the particle. By contrast, the high (dis)charge rate tends to decrease the SOC of Si–Gr composite anode, leading to small volume change and von Mises stress of the cell.

As discussed above, the composite of Si and Gr can appropriately compensate for their respective limitations. Still, the influence of Si content on electrochemical behavior and stress of each active material in the anode necessitate further investigation. As shown in Fig. 4(a), the turning point of the lithiation curve of Gr during charge is delayed with the increment of Si content, while is pushed forward during the discharge. In comparison, the SOL of Si decreases, and the plateau disappears as the Si content increases (Fig. 4(b)). Specifically, as the Si content increases from 5.5 wt% to 21 wt%, the SOC contribution of graphite during charge decreases from 60% to 28% (Fig. 4(c)), while the SOC contribution of Si increases from 32% to 64% (Fig. 4(d)). It is obvious that the (de)lithiation behavior of Si is gradually dominated as the Si content increases. In addition, the increment of Si content significantly increases the volume change of the cell and the corresponding stress (Fig. 4(e)). By comparison, the stress of the particle is reduced with the increase of Si content

(Fig. 4(f)), because the rise in Si content minimizes the thickness of the negative electrode, thereby reducing the internal polarization of the electrode and ensuring the concentration uniformity in the particle. Accordingly, there is a tradeoff between the volume change and capacity in the Si–Gr composite anode when Si content changes.

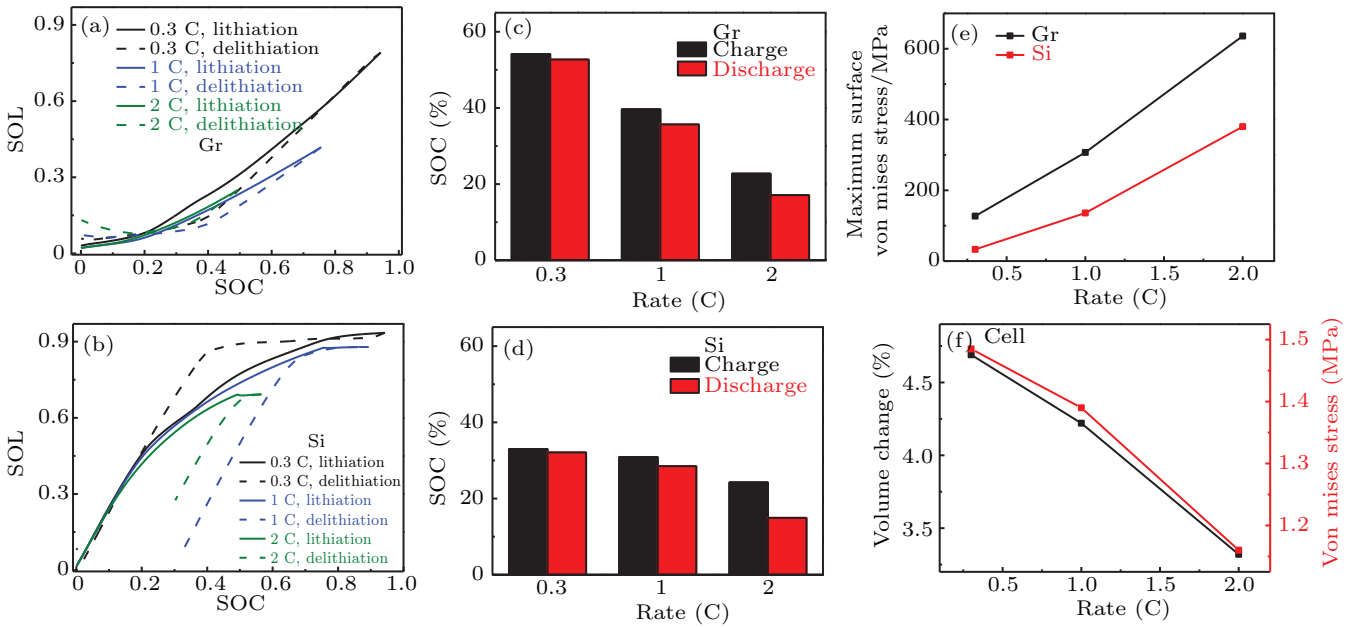


Fig. 3. Effect of (dis)charge rate on the electrochemical behavior of SiGr composite anode (with 5.5 wt% Si). The SOL of (a) Gr and (b) Si, the SOC contribution of (c) Gr and (d) Si, (e) the surface stress of particle, and (f) the von Mises stress and volume change of the cell in the different (dis)charge rate.

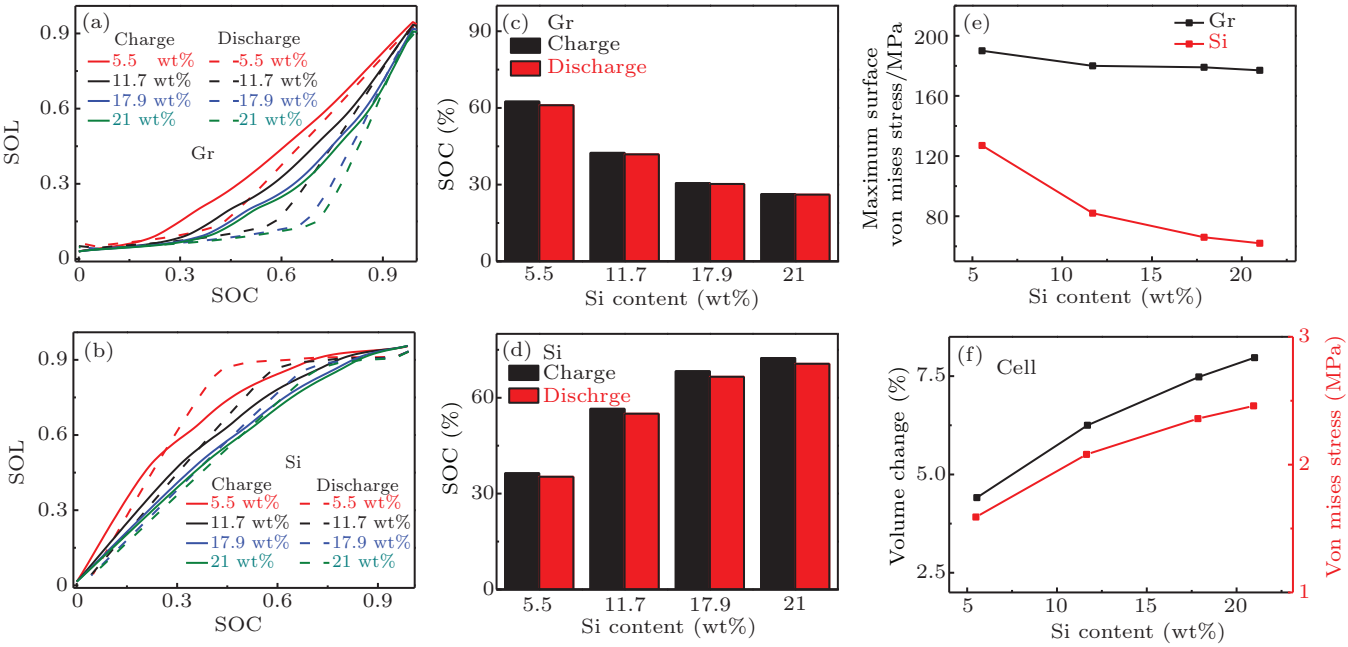


Fig. 4. Effect of Si content on the electrochemical behavior of Si–Gr composite anode at 0.3 C. The SOL state of (a) Gr and (b) Si, the SOC contribution of (c) Gr and (d) Si, (e) the surface stress of particle, (f) the volume change and von Mises stress of the cell in different Si content.

As mentioned above, both the charge rate and Si content will affect the negative electrode potential during the charging process. Generally, the negative electrode potential below 0 V is directly an indicator of the lithium plating behavior on the negative side. Therefore, the influence of the charge rate and Si content on the lithium plating at the negative electrode is explored in Fig. 5. Figure 5(a) shows that the electrode potential at the side of the separator is lower than the side of the current collector. This is because the electrolyte ohmic drop and electrolyte diffusion polarization cause lower liquid phase potential at the separator side compared with the current collector side during charge. By comparison, the solid phase potential has no obvious changes. This results in a lower electrode potential on the separator side. As the charge rate increases, the electrode potential at the separator side decreases. Specifically, the separator side is already less than 0 V at a current

rate above 1 C, whereas the current collector side is not less than 0 V even at 2 C. This indicates that the separator side is prone to lithium plating.[37] As for the effect of Si content on the Li plating at the negative electrode, Fig. 5(b) shows that the increment of Si content in the Si–Gr composite anode enhances the electrode potential of the negative electrode. These results indicate that increasing the Si content and decreasing the charge rate can reduce the risk of lithium plating behavior.

The polarization of the battery during (dis)charge directly affects the battery's capacity and heat generation inside the cell. Therefore, decomposing the polarization inside the cell is helpful to understand the overall performance of the Si-based LIBs. Generally, the polarization of the battery is mainly divided into the two domains: the anode and cathode as shown in Fig. 6. The polarization from each of the five subprocesses at 1 C is displayed in Figs. 6(a) and 6(b). Initially, the polarization is dominated by the activation overpotential of Si and NCM811. These activation overpotential decrease as SOC increases. Meanwhile, the Gr activation overpotential, electrolyte diffusion and ohmic polarization increase slightly. The polarization relative contributions at different charge rates and SOC = 0.5 are further analyzed, as shown in Figs. 6(c) and 6(d). The anode contributes more than the cathode at all charge rates. The Gr activation is more important and increases somewhat as the charge rate increases in the anode (Fig. 6(c)), which is in line with the indications of Fig. 6(a). In contrast, the cathode is considerably more polarized by the electrolyte ohmic and diffusion polarization (Fig. 6(d)). Therefore, the rate performance of the lithium-ion battery with Si–Gr anode is dominated by the subprocess of Gr activation and liquid phase polarization. It can be improved by regulating the surface electrochemical dynamics of Gr such as coating[38] and reducing the liquid phase polarization such as using high ionic conductivity electrolytes or increasing the porosity of the positive electrode side to reduce the liquid phase polarization.

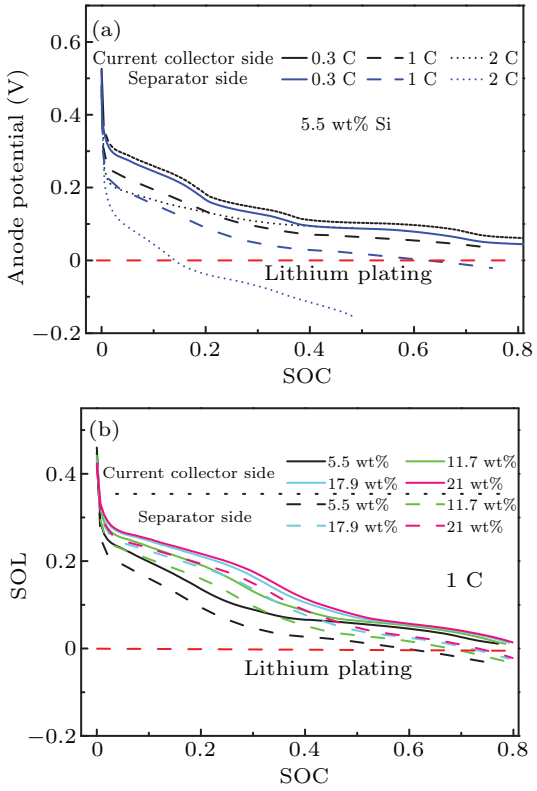


Fig. 5. Effects of (a) rate and (b) Si content on lithium plating in the negative electrode.

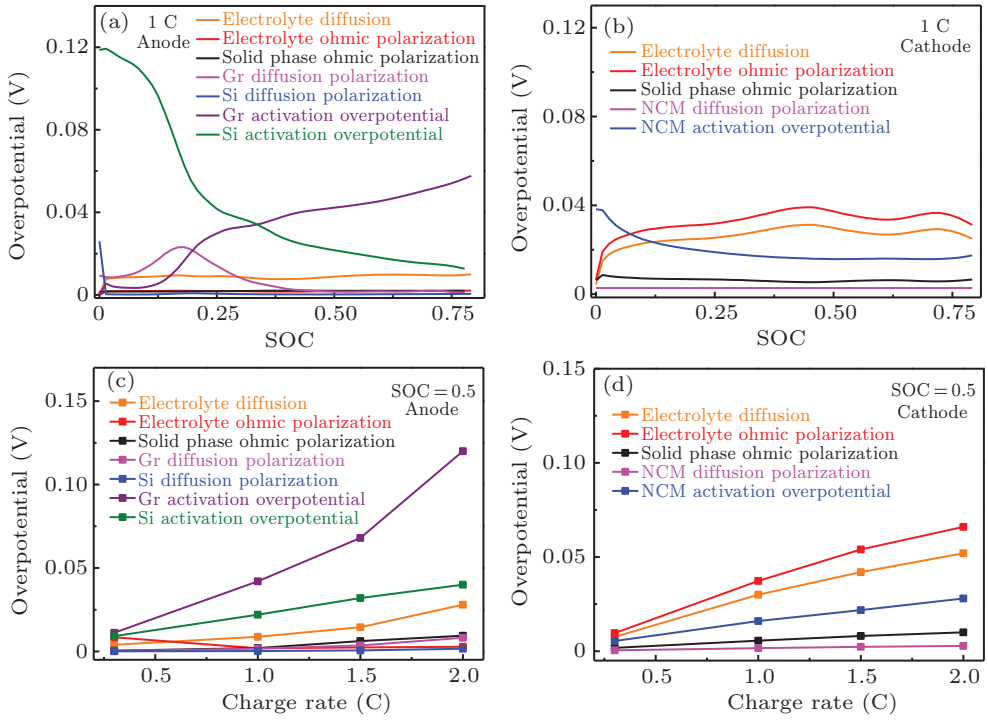


Fig. 6. Polarization decomposition and proportion of Si–Gr 550/NCM811 cells during charge. The polarization decomposition of (a) anode and (b) cathode during 1 C charge. The trend of polarization of (c) anode and (d) cathode with the different charge rates.

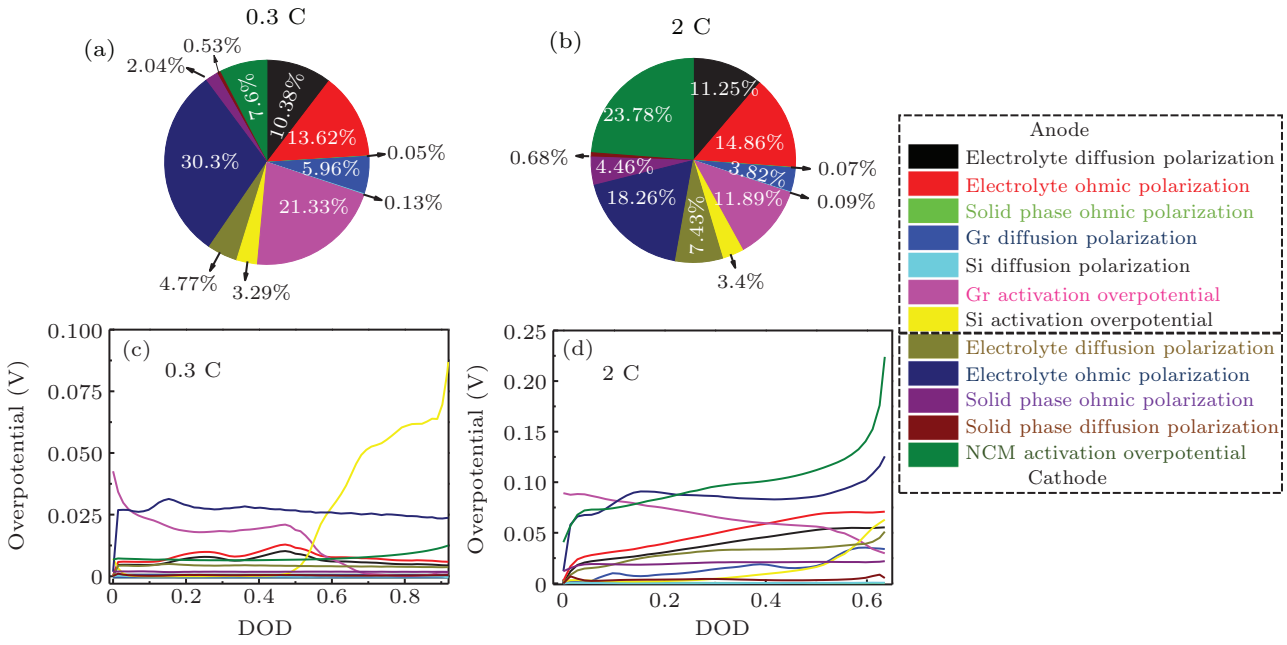


Fig. 7. Polarization proportion and decomposition of Si–Gr 550/NCM811 cells during discharge. Polarization proportion of Si–Gr 550/NCM811 cells at SOC = 0.5 at (a) 0.3 C and (b) 2 C. Polarization decomposition of Si–Gr 550/NCM811 cells at discharge rate of (c) 0.3 C and (d) 2 C.

The limiting factors for the power performance of Si-based anode system cells are explored through voltage decomposition. The relative polarization contributions (SOC = 0.5) at 0.3 C and 2 C are shown in Figs. 7(a) and 7(b). The anode and cathode contribute 54.76% and 45.24% of polarization at 0.3 C, respectively, whereas the cathode contributions are more important than the anode, 53.93% and 46.07% at 2 C, respectively. Specifically, the anode is considerably more polarized by graphite activation and electrolyte ohmic polarization at 0.3 C and 2 C. In contrast, electrolyte ohmic polarization and NCM811 activation overpotential are more critical in the cathode at 0.3 C and 2 C, respectively. Moreover, when the discharge rate is increased from 0.3 C to 2 C, the polarization contribution of NCM811 activation overpotential increases from 7.6% to 23.78%, whereas electrolyte ohmic polarization decreases from 30.3% to 18.26%. This indicates that NCM811 activation overpotential and electrolyte ohmic polarization are sensitive to discharge rate. In Fig. 7(c), it can be seen that the polarization is dominated by activation over-potential of Gr at the initial discharge stage. As the SOC increases, the ohmic polarization of electrolyte and the activation overpotential of Si and NCM811 increase, whereas the activation overpotential of Gr decreases at 0.3 C. Notably, the activation overpotential of Si has low occupation at SOC = 0.5 (Fig. 7(a)). In contrast, it plays a major role in polarization contributions at the end of discharge. In addition, NCM activation and electrolyte ohmic overpotential increase obviously and contribute to dominated polarization at 2 C (Fig. 7(d)), which is in line with the indications of Fig. 6(a). Thus, to improve the power performance of the cell, the strategies reducing the electrochemical polarization of the NCM, such as the coating method[39] and transition metal doping,[40] can be applied.

4. Conclusions

In summary, an electrochemical-mechanical coupled model is established with considering the independent electrochemical behavior of Si and Gr to investigate the electrochemical behavior and stress behavior of the Si–Gr composite anode. The model is validated by experimental evidence with Si–Gr/NMC811 cells. The SOC and SOL evolution of Si and Gr during (dis)charge is further analyzed via this model. Then, the effect of the rate and Si content of Si–Gr composites on the electrochemical performance and Li plating behavior of the composite anode is discussed. The results indicate that the composite of Si and Gr improves lithiation kinetics of Gr and alleviates the voltage hysteresis of Si. What's more, there is a tradeoff between the volume change and capacity in the Si–Gr composite anode when Si content changes. The polarization of the LIBs based on the Si–Gr composite anode is quantified by the voltage decomposition method. It is demonstrated that the rate performance is dominated by the electrochemical polarization of anode and cathode and the electrolyte ohmic polarization. Thus, improving these two directions is the key to solving cell rate performance.

Appendix A

Table A. Glossary.

ε	volume fraction
j	flux of lithium ions ($\mathrm{mol\cdot m^{-2}\cdot s^{-1}}$)
D	diffusion coefficient of lithium ions ($\mathrm{m^2\cdot s^{-1}}$)
c	concentration of lithium ions in the active material ($\mathrm{mol\cdot m^{-3}}$)
R	universal gas constant ($\mathrm{J\cdot mol^{-1}\cdot K^{-1}}$)
T	Kelvin temperature (K)
μ	chemical potential of Li-ion in the active material ($\mathrm{J\cdot mol^{-1}}$)
Ω	partial molar volume of the active material ($\mathrm{m^3\cdot mol^{-1}}$)
σ	stress (Pa)
F	Faraday's constant ($\mathrm{C\cdot mol^{-1}}$)
E_{ref}	reference electrode potential (V)
x	Li-ion mole fraction in the active material
i	current density ($\mathrm{A\cdot m^{-2}}$)
r	radius (m)
e	strain
C_{ijkl}	elastic stiffness tensor
Σ_{ij}	stress tensor
δ	Kronecker delta
V	volume ($\mathrm{m^3}$)
f	volume change fraction
u	displacement (m)
E	Young's modulus (Pa)
G	shear modulus (Pa)
λ	Lame constant
v	Poisson's ratio
k	reaction rate constant ($\mathrm{m^2\cdot s^{-1}}$)
a	specific surface area of active material ($\mathrm{m^{-1}}$)
φ	potential (V)
t_+	transference number
ρ	density of active material ($\mathrm{kg\cdot m^{-3}}$)
M	molar mass ($\mathrm{g\cdot mol^{-1}}$)
w	mass fraction
Q	active material specific capacity ($\mathrm{mAh\cdot g^{-1}}$)

Acknowledgements

Project supported by the National Key Research and Development Program of China (Grant No. 2019YFE0100200), the National Natural Science Foundation of China (Grant No. U1964205), and the Beijing Municipal Science and Technology Commission (Grant No. Z191100004719001).

References

[1] Duffner F, Kronemeyer N, Tubke J, Leker J, Winter M and Schmuch R 2021 *Nat. Energy* **6** 123
[2] Radin M D, Hy S, Sina M, Fang C C, Liu H D, Vinckeviciute J, Zhang M H, Whittingham M S, Meng Y S and Van der Ven A 2017 *Adv. Energy Mater.* **7** 1602888
[3] Xia Y, Zheng J M, Wang C M and Gu M 2018 *Nano Energy* **49** 434
[4] Zuo C J, Hu Z X, Qi R, Liu J J, Li Z B, Lu J L, Dong C, Yang K, Huang W Y, Chen C, Song Z B, Song S C, Yu Y M, Zheng J X and Pan F 2020 *Adv. Energy Mater.* **10** 2000363
[5] Xu C Y, Li J L, Feng X Y, Zhao J W, Tang C J, Ji B M, Hu J, Cao C B, Zhu Y Q and Butt F K 2020 *Electrochim. Acta* **358** 136901
[6] Wenjun L 2020 *Energy Storage Sci. Technol.* **9** 448 (in Chinese)
[7] Yao K P C, Okasinski J S, Kalaga K, Almer J D and Abraham D P 2019 *Adv. Energy Mater.* **9** 1803380
[8] Berhaut C L, Dominguez D Z, Kumar P, Jouneau P H, Porcher W, Aradilla D, Tardif S, Pouget S and Lyonnard S 2019 *Acs Nano* **13** 11538
[9] Richter K, Waldmann T, Paul N, Jobst N, Scurtu R G, Hofmann M, Gilles R and Wohlfahrt-Mehrens M 2020 *ChemSusChem* **13** 529
[10] Moon J, Lee H C, Jung H, Wakita S, Cho S, Yoon J, Lee J, Ueda A, Choi B, Lee S, Ito K, Kubo Y, Lim A C, Seo J G, Yoo J, Lee S, Ham Y, Baek W, Ryu Y G and Han I T 2021 *Nat. Commun.* **12** 2714
[11] Heubner C, Liebmann T, Lohrberg O, Cangaz S, Maletti S and Michaelis A 2021 *Batteries & Supercaps* **5** e202100182
[12] Chandrasekaran R, Magasinski A, Yushin G and Fuller T F 2010 *J. Electrochem. Soc.* **157** A1139
[13] Chandrasekaran R and Fuller T F 2011 *J. Electrochem. Soc.* **158** A859
[14] Smith R B, Khoo E and Bazant M Z 2017 *J. Phys. Chem. C* **121** 12505
[15] Chandesris M, Caliste D, Jamet D and Pochet P 2019 *J. Phys. Chem. C* **123** 23711
[16] Liu B H, Jia Y K, Li J N, Jiang H Q, Yin S and Xu J 2020 *J. Power Sources* **450** 227667
[17] Liu B H, Wang X, Chen H S, Chen S, Yang H X, Xu J, Jiang H Q and Fang D N 2019 *J. Appl. Mech.-Trans. Asme* **86** 041005
[18] Pereira D J, Weidner J W and Garrick T R 2019 *J. Electrochem. Soc.* **166** A1251
[19] Lory P F, Mathieu B, Genies S, Reynier Y, Boulineau A, Hong W and Chandesris M 2020 *J. Electrochem. Soc.* **167** 120506
[20] Zhuang Y, Zou Z Y, Lu B, Li Y J, Wang D, Avdeev M and Shi S Q 2020 *Chin. Phys. B* **29** 068202
[21] Doyle M and Newman J 1995 *Electrochim. Acta* **40** 2191
[22] Christensen J and Newman J 2006 *J. Electrochem. Soc.* **153** A1019
[23] Christensen J and Newman J 2006 *J. Solid State Electrochem.* **10** 293
[24] Nyman A, Zavalis T G, Elger R, Behm M and Lindbergh G 2010 *J. Electrochem. Soc.* **157** A1236
[25] Sturm J, Rheinfeld A, Zilberman I, Spingler F B, Kosch S, Frie F and Jossen A 2019 *J. Power Sources* **412** 204
[26] Doyle M, Newman J, Gozdz A S, Schmutz C N and Tarascon J M 1996 *J. Electrochem. Soc.* **143** 1890
[27] Li H G, Liu B H, Zhou D and Zhang C 2020 *J. Electrochem. Soc.* **167** 120501
[28] Pan K, Zou F, Canova M, Zhu Y and Kim J H 2019 *J. Power Sources* **413** 20
[29] Louli A J, Li J, Trussler S, Fell C R and Dahn J R 2017 *J. Electrochem. Soc.* **164** A2689
[30] Chevrier V L and Dahn J R 2009 *J. Electrochem. Soc.* **156** A454
[31] Sethuraman V A, Chon M J, Shimshak M, Srinivasan V and Guduru P R 2010 *J. Power Sources* **195** 5062
[32] Baggetto L, Niessen R A H, Roozeboom F and Notten P H L 2008 *Adv. Funct. Mater.* **18** 1057
[33] Vidal D, Leys C, Mathieu B, Guillet N, Vidal V, Borschneck D, Chaurand P, Genies S, De Vito E, Tulodziecki M and Porcher W 2021 *J. Power Sources* **514** 230552
[34] Yu P, Popov B N, Ritter J A and White R E 1999 *J. Electrochem. Soc.* **146** 8
[35] McDowell M T, Lee S W, Harris J T, Korgel B A, Wang C M, Nix W D and Cui Y 2013 *Nano Lett.* **13** 758
[36] de Vasconcelos L S, Xu R and Zhao K J 2020 *J. Mech. Phys. Solids* **144** 104102
[37] Mei W X, Jiang L H, Liang C, Sun J H and Wang Q S 2021 *Energy Storage Mater.* **41** 209
[38] Kim J, Jeghan S M N and Lee G 2020 *Microporous Mesoporous Mater.* **305** 110325
[39] Sattar T, Sim S J, Jin B S and Kim H S 2021 *Sci. Rep.* **11** 18590
[40] Jung C H, Shim H, Eum D and Hong S H 2021 *J. Korean Ceram. Soc.* **58** 1